International Journal of Fatigue 203 (2026) 109252

Contents lists available at ScienceDirect

International Journal of Fatigue

journal homepage: www.elsevier.com/locate/ijfatigue

Comparison of methods for the determination of fatigue critical flaw size and implementation for probabilistic fatigue assessment

Lorenzo Rusnati [a], Giuliano Minerva [a], Luca Patriarca [a], Stefano Miccoli [a], Stefano Beretta [a,b,*]

[a] Politecnico di Milano, Department of Mechanical Engineering, via La Masa 1, 20156 Milano, Italy
[b] Auburn University, National Center for Additive Manufacturing Excellence (NCAME), Auburn, Al 36849, USA

ARTICLE INFO

Keywords:
Additive manufacturing
Fatigue assessment
Fracture mechanics
Critical flaw size
Failure probability

ABSTRACT

The correct evaluation of the impact of defects in the structural integrity of metal additively manufactured components is a necessary step to be addressed for the broader adoption of the additive manufacturing technology. The effect of flaws on fatigue strength of materials can be evaluated through different theoretical approaches, among which fracture mechanics-based theory was successfully applied in several applications. However, each method presents notable differences which alter the life estimates of parts. Therefore, in this work, the authors compare the fatigue life predicted by four different methods against results from a wide fatigue test campaign on Ti-6Al-4V specimens in different conditions. Then, critical defect size curves, identifying the stress–defect–life relation from each of the analysed model, are established and critically evaluated. Finally, the fatigue strength model based on explicit crack growth analysis, which is the standard assessment method for fracture control, is implemented in ProFACE software. This allows to determine the critical initial flaw size in probabilistic fatigue analyses of components, addressing different geometries and materials.

1. Introduction

Defects are one of the main factors ruling the uncertainty in fatigue properties of additively manufactured (AM) metals. With reference to the laser powder bed fusion (PBF-LB) process, pores, keyholes and lacks-of-fusion (LoFs) are the most common material volumetric anomalies [1]. Their formation is due to an unbalanced volumetric energy density: for keyholes and gas-entrapped pores, a large volumetric energy density causes the melt pool to leave a void, whereas for LoFs only partial melting of the metal powder occurs [2,3]. The presence of these embedded flaws may affect both static and, particularly, fatigue properties of the material [4,5]. Similarly, surface defects harm the fatigue properties of AM parts [6,7], especially for net-shape components. Surface features, in fact, act as stress raisers and thus foster the nucleation and propagation of cracks under cyclic loading [8–10].

Anomalies' formation and impact can be reduced through advanced printing strategies and tailored post-processes [4,11,12]. However, their presence must be accounted for from the structural integrity assessment perspective [13]. In this field, fracture mechanics theory plays a major role in the assessment of defects. A first approach to analyse defects in AM materials was the use of the Kitagawa–Takahashi (KT) diagram [14,15]. The KT diagram [16] expresses the transition from fatigue resistance of long cracks, ruled by linear elastic fracture mechanics (LEFM), to microstructurally and to physically short cracks, linked to the endurance limit of the material. A formulation of the fatigue limit for short cracks was originally elaborated by El-Haddad et al. [17], who introduced the l_0 parameter to model the transition between the two regimes. Murakami [18] found that fatigue limit was proportionally linked to the Vickers hardness of the material, while being inversely proportional to $(\sqrt{\text{area}})^{1/6}$, considering the area of the projection of the defect onto the plane perpendicular to the maximum tensile stress direction.

The fatigue limit in the KT diagram is associated to a critical defect size considering an infinite life. However, within the assessment of components in a defect tolerance perspective, it is necessary to evaluate flaws based on a finite service life. This requires the derivation of critical defect curves, which express the relation among the applied stress, the size of anomalies and the target life [19].

A first example of these relations is based on the normalization of the S–N curves. In the work by Murakami [20], the applied stress of S–N curves was normalized with the fatigue limit computed for the defect size related to the specimen. In later works, Murakami et al. [21] implemented this approach for metal AM, discussing the correlation

* Corresponding author at: Politecnico di Milano, Department of Mechanical Engineering, via La Masa 1, 20156 Milano, Italy.
E-mail address: stefano.beretta@polimi.it (S. Beretta).

https://doi.org/10.1016/j.ijfatigue.2025.109252
Received 9 May 2025; Received in revised form 1 August 2025; Accepted 23 August 2025
Available online 6 September 2025

Nomenclature

Acronyms

AM	additive manufacturing
AR	aspect ratio
FE	finite element
FCG	fatigue crack growth
KT	Kitagawa-Takahashi
LEFM	linear elastic fracture mechanics
LEVD	largest extreme value distribution
LoF	lack-of-fusion
ML	machine learning
PBF-LB	laser powder bed fusion
SEM	scanning electron microscopy
SIF	stress intensity factor
VHCF	very high cycle fatigue

Symbols

α	constraint factor
δ	scale parameter of the LEVD
ΔF	force range
ΔK	applied SIF range
$\Delta K_{\mathrm{th,LC}}$	long crack threshold SIF range
ΔK_{th}	threshold SIF range
ΔK_1	parameter of the NASGRO equation
$\Delta\sigma$	applied stress range
$\Delta\sigma_0$	fatigue strength stress range for defect-free material
$\Delta\sigma_{\mathrm{w},0}$	fatigue limit stress range for defect-free material
$\Delta\sigma_{\mathrm{w}}$	fatigue limit stress range
λ	position parameter of the LEVD
σ_ϵ	scatter of the fatigue life model
$\sigma_{\log(\Delta\sigma_{\mathrm{w},0})}$	standard deviation of $\log(\Delta\sigma_{\mathrm{w},0})$
$\sigma_{\log(\Delta K)}$	standard deviation of $\log(\Delta K)$
σ_{flow}	flow stress
σ_{max}	maximum stress
$\sigma_{\mathrm{net,max}}$	maximum net stress
σ_{RS}	residual stress
$\sqrt{\mathrm{area}}$	defect size as Murakami's parameter
$\sqrt{\mathrm{area}}_0$	El-Haddad's parameter expressed as defect's projected area
$\sqrt{\mathrm{area}}_{50\%}$	average defect size
$\sqrt{\mathrm{area}}_i$	initial defect size
$\sqrt{\mathrm{area}}_f$	final defect size
a	crack depth
A_0	parameter of the NASGRO equation
a_{crit}	critical crack size
a_f	final crack length
a_i	initial crack length
c	crack width
C	parameter of the NASGRO equation
C^*	parameter of the Murakami's FCG law
C_{th}^-	parameter of the NASGRO equation
C_{th}^+	parameter of the NASGRO equation
C_0	parameter of the Sheridan's fit
C_1	parameter of the Sheridan's fit
C_2	parameter of the Sheridan's fit
$\mathrm{CV}_{\Delta\sigma_{\mathrm{w},0}}$	coefficient of variation of the fatigue strength
d'	parameter of the Shiozawa's fit
f	probability density function
F_{LEVD}	cumulative density function of the LEVD
f_N	Newman's crack closure function
f_w	correction factor for finite-width section
k_σ	parameter of the S–N curve
K_a	SIF at the deepest point of a semi-elliptical crack
K_c	SIF at the surface point of a semi-elliptical crack
K_{RS}	SIF induced by residual stresses
K_{Ic}	fracture toughness
K_{max}	maximum SIF
K_f'	parameter of the Shiozawa's fit
l_0	El-Haddad's parameter
m	parameter of the NASGRO equation
m^*	parameter of the Murakami's FCG law
$M_{1A}/M_{2A}/M_{3A}$	coefficient of the weight function for crack tip A
$M_{1B}/M_{2B}/M_{3B}$	coefficient of the weight function for crack tip C
N	number of fatigue cycles
n^*	parameter of the Murakami's FCG law
N_{calc}	predicted fatigue life
N_{exp}	experimental fatigue life
N_f	number of fatigue cycles to failure
N_k	parameter of the S–N curve
p	parameter of the NASGRO equation
q	parameter of the NASGRO equation
$\mathcal{R}$	reliability
R	stress ratio
R_{eff}	effective stress ratio
S_{app}	applied stress
t	section depth
UTS	ultimate tensile strength
V	volume
V_s	sampling volume
w	section width
Y	shape factor

among S–N curves for different defect sizes. The normalized stress was recognized as the main driving force for crack growth in the work of Murakami and Endo [22]. The normalized S–N approach, in combination with El-Haddad model, has been employed by Romano et al. [23] to describe fatigue tests of different batches of specimens onto a single S–N curve irrespective of the defect size.

Rather than S–N curves, it is not uncommon to visualize the fatigue life in relation to the applied stress intensity factor (SIF), hence in K–N diagrams. In various cases, these curves have shown a lower scatter in fatigue life [24,25]; other works [26], however, highlighted that a strong improvement in the fit can only be obtained with the normalization of the cyclic SIF, effectively creating an analogous expression to the one by Murakami. Sheridan et al. [25] implemented the K–N plot towards a fatigue assessment method and employed the correlation to develop a stress–defect–life description.

The use of the applied SIF to identify a more effective relation to fatigue data was also explored by Shiozawa and Lu [27,28] to study the gigacycles fatigue regime; they proposed a correlation between

the applied SIF and the fatigue cycles per unitary initial crack length. Tenkamp et al. [29] employed this relation to show that a single curve was able to fit the experimental data from high cycle fatigue tests pertaining to a particular defect configuration, independently of the size of the critical flaw. Similar results were obtained on titanium aluminides [30] and on AlSi10Mg specimens [31].

Another well-established methodology for the assessment of defects is the use of fatigue crack growth (FCG) algorithms to determine the prospective fatigue life. This fracture mechanics-based approach, indeed, is prescribed by NASA and ESA in fracture control standards for the deterministic assessment of material anomalies [32,33]. Yadollahi et al. [34] described the fatigue behaviour of PBF-LB/Inc718 using the FCG law related to the plasticity-induced crack closure model FASTRAN for surface anomalies. Sanaei and Fatemi [35] and Kishore et al. [36] employed the Hartman-Schijve variation of the NASGRO equation to derive the prospective life of Ti-6Al-4V parts.

Fracture mechanics-based approaches have been increasingly coupled with machine learning (ML) methods to construct robust physics-informed models. Within these approaches, ML techniques are employed with well-established fracture mechanics laws, such as the definition of the SIF or a FCG equation, and prove to well represent the actual fatigue behaviour of samples [26,37–40]. However, ML-assisted methods are currently not considered in fracture control standards by ESA and NASA [32,33].

A typical use of critical flaw size curves is their implementation in probabilistic assessment of a component. The scientific literature shows different types of implementation for probabilistic defect tolerance analyses. A branch of these models is based on a weakest-link approach applied to Weibull statistics [41–43], in which the defect size distribution is related to the fatigue strength distribution. Other works introduce an explicit calculation of the probability of failure from a stress–defect–life relation. In [44,45], the FE post-processor software P-FAT performs explicit FCG analyses in combination with Monte Carlo simulations to derive the fatigue life distribution of a part. DARWIN software [46–48] exploits Monte Carlo simulations to perform crack propagation analyses coupled with defect detection simulations. The use of critical flaw size, calculated with the normalized S–N method, is the basis for a weakest-link approach in combination with extreme value statistics within ProFACE software [49,50].

The aim of this paper is to critically compare the four different fatigue strength models based on fracture mechanics concepts. Their performance is firstly evaluated by comparing the resulting life estimates with the experimental fatigue data of three series of Ti-6Al-4V samples. The models are then utilized to determine critical defect curves. Then, an implementation of fatigue critical defect curves, based on explicit crack growth analysis, is shown. Finally, the method is implemented in ProFACE software to provide improved fatigue life estimates for PBF-LB benchmark components manufactured with AlSi10Mg alloy.

2. Experimental database

2.1. Ti-6Al-4V test articles

The experimental campaign conducted on Ti-6Al-4V specimens was performed and reported by some of the authors in [51]. Fatigue and crack propagation specimens were manufactured by PBF-LB with the Renishaw AM500Q system. The parts were thermally treated at 650 °C for 2 h, followed by furnace cooling; the heat treatment removed the residual stresses induced by the PBF-LB process.

Fatigue specimens were grouped in two batches based on their surface condition: one set of specimens was tested in net-shape surface condition, the other set was electro-chemically milled by the Hirtisation® process prior to testing. The preparation of the specimens and the outcome of the high cycle fatigue tests on the two series has been extensively reported and analysed in [51]. Such data are also reported in Appendix. In addition to the mentioned work, fatigue specimens with micro-notches (0.1 mm depth × 1 mm surface length and height of 0.1 mm) were subjected to fatigue tests at $R = -1$ with the MTS 810 servo-hydraulic equipment which had been used for the other series.

Table 1
Average geometrical characteristics of Ti-6Al-4V failure initiation defects from fractography, from [51].

Sample type	$\sqrt{area}_{50\%}$	Average AR	λ	δ
Net-shape	98 µm	0.2	88 µm	26 µm
Chemically milled	72 µm	1	66 µm	16 µm
Micro-notched	186 µm	0.9	–	–

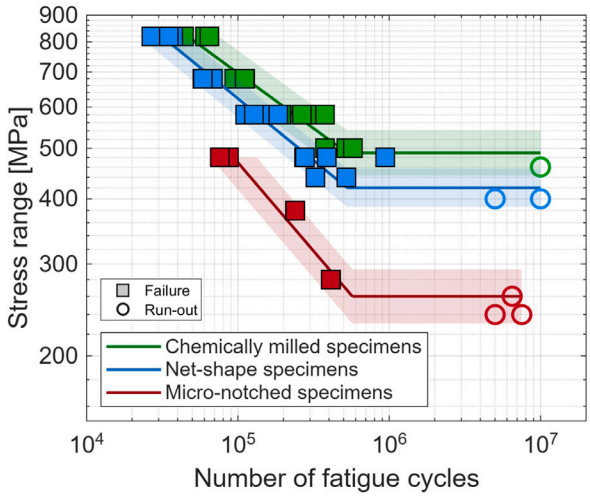

Fig. 1. Fatigue properties of the three series Ti-6Al-4V specimens adopted for this analysis, from [51].

The results of the fatigue tests are reported in Fig. 1, along with the fits of the S–N curves and the 95 % scatter bands. After the completion of the tests, fracture surfaces imaging via scanning electron microscopy (SEM) revealed the failure initiation defects, which were observed to be surface or sub-surface anomalies in each specimen and were measured in terms of $\sqrt{area}$ and aspect ratio (AR); $\sqrt{area}$ is defined as the square root of the area of the defect projected onto the plane normal to the direction of the maximum principal stress; whereas the aspect ratio is the ratio between the depth and half-width of a surface flaw. The critical initial flaw sizes of net-shape and chemically milled specimens were analysed with the extreme value statistics and thus fitted with the largest extreme value distribution (LEVD), whose cumulative density function is:

$$F_{\mathrm{LEVD}}(\sqrt{area}) = \exp\left[-\exp\left(-\frac{\sqrt{area}-\lambda}{\delta}\right)\right] \quad (1)$$

in which λ is the position parameter and δ is the scale parameter, both obtained with the moments' method [52]. For micro-notched specimens only the defect size $\sqrt{area}_{50\%}$ and AR were collected. Table 1 reports the values related to the failure initiation defects for all the specimens considered in the study.

2.2. AlSi10Mg benchmark components

The activity conducted in 2022 by Beretta et al. [53] and by Sausto et al. [50] involved the manufacturing, testing and assessment of a large number of AlSi10Mg articles. The core of the activity concerned the wishbone-shaped benchmark components, manufactured by PBF-LB

and depicted in Fig. 2a in terms of maximum principal stress for a 1 kN tensile load from FE analysis. Half of the 32 manufactured items were left in net-shape condition, whereas the other half were fully machined. No thermal treatment was performed on the components. In the same builds, fatigue and FCG specimens were manufactured to characterize the properties of the alloy.

The present work focuses on the net-shape components. Due to the lack of heat treatments and surface finishing operations, the parts maintained notable tensile residual stresses, whose profile beneath the surface is displayed in Fig. 2b. For the analysis of AlSi10Mg components, this study considers the following data from the referenced experimental campaign, which are also reported in Appendix: (i) fatigue tests on the net-shape cylindrical specimens conducted at $R = 0.1$, (ii) crack propagation tests at different stress ratios and subsequent NASGRO fit, (iii) the residual stress measurements on the benchmark components and (iv) the results of the fatigue tests on the components at $R = 0.1$ (Fig. 2c).

In addition, SEM was employed for the observation of the fracture surfaces of the components. As reported in [53], the LEVD (1) was fitted to the sizes of the failure initiation defects. The median defect $\sqrt{\text{area}}_{50\%}$ had a size of 242 µm, whereas the distribution of defects had parameters $\lambda = 211$ µm and $\delta = 85$ µm. The average AR was equal to 0.4.

3. Application of fatigue life models to Ti-6Al-4V database

This Section introduces the fatigue strength models showing their application to the Ti-6Al-4V alloy fatigue dataset. The methods are discussed from their constitutive equations, required inputs and constraints. Their agreement with experimental data will be then addressed in Section 4, with a comparison of the fatigue life estimates for the average defect.

3.1. Fatigue strength model by normalized S–N curve

Within the normalized S–N approach, the fatigue strength is evaluated from the KT diagram constructed applying the El-Haddad model (2) with the defect size formulated as the Murakami's $\sqrt{\text{area}}$:

$$\Delta\sigma_w = \Delta\sigma_{w,0} \cdot \sqrt{\frac{\sqrt{\text{area}}_0}{\sqrt{\text{area}}_0 + \sqrt{\text{area}}}} \tag{2}$$

$$\sqrt{\text{area}}_0 = \frac{1}{\pi}\left(\frac{\Delta K_{th,LC}}{Y \cdot \Delta\sigma_{w,0}}\right)^2 \tag{3}$$

where $\Delta\sigma_w$ is the fatigue limit stress range, $\Delta\sigma_{w,0}$ is the fatigue limit stress range in absence of defects, Y is the crack geometric factor and $\Delta K_{th,LC}$ is the long crack threshold SIF range. To express the material strength at finite fatigue life, the KT diagram is combined with the relation expressing the log-linear dependency between normalized stress and life:

$$\frac{\Delta\sigma(N)}{\Delta\sigma_w} = \left(\frac{N}{N_k}\right)^{-1/k_\sigma} \tag{4}$$

in which N_k is the number of cycles related to the fatigue limit and k_σ is the slope of the normalized S–N curve in its finite region. It is thus possible to have an analytical description of fatigue strength at variable fatigue life as a function of the critical initial flaw size:

$$\Delta\sigma(N) = \Delta\sigma_{w,0}\left(\frac{N}{N_k}\right)^{-1/k_\sigma}\sqrt{\frac{\sqrt{\text{area}}_0}{\sqrt{\text{area}}_0 + \sqrt{\text{area}}}} \tag{5}$$

Fig. 3a shows the KT diagram along with the experimental points from the fatigue tests of Ti-6Al-4V alloy. The stress levels of the three series of Ti-6Al-4V specimens were normalized employing the fatigue limit derived from Eq. (2), considering $\Delta\sigma_{w,0} = 0.8 \cdot \text{UTS}$ [54], $Y = 0.65$ (i.e. surface flaws), and the size of flaw as observed by SEM. The values of N_k and k_σ were then determined as the average among the three series, weighted for the numerousness of the samples, and are equal to 533290 and 4.238, respectively. The normalized experimental points and the resulting S–N curve are depicted in Fig. 3b. To maintain a conservative approach for fatigue cycles in the very-high cycle fatigue (VHCF) region, a second slope may be implemented on the normalized S–N curve; this choice is reflected in the gray hatched area in Fig. 3. Considering the experimental data on structural alloys [55], a VHCF slope k_σ equal to 22 was assumed for the Ti-6Al-4V specimens.

Murakami et al. [21,22,56] proposed an additional interpretation of the normalization of the S–N curve, with the aim of describing a crack propagation law:

$$\frac{da}{dN} = C^*\left(\frac{\Delta\sigma}{\Delta\sigma_w} - 1\right)^{m^*}\left(\sqrt{\text{area}}\right)^{n^*} \tag{6}$$

in which C^*, m^* and n^* are model coefficients, whereas $\Delta\sigma_w$ is computed with Eq. (2). In his works, Murakami stated that the three coefficients are equal to 1×10^{-4}, -2 and 1 respectively, regardless of the material. The propagation was numerically solved from the average defect size up to a maximum crack size $\sqrt{\text{area}}$ equal to 2 mm. This is consistent with the extent of the stable crack advancement observed on the fracture surfaces of the specimens. The results are displayed in Fig. 3b. Murakami's FCG law follows the same slope of the experimental data, although it is over-conservative in the finite life region.

3.2. Fatigue strength model proposed by Sheridan

In accordance with the proposal by Sheridan et al. [25], the applied SIF range for the derivation of the K–N plot was computed with the Murakami's $\sqrt{\text{area}}$ parameter:

$$\Delta K = Y\Delta\sigma\sqrt{\pi\sqrt{\text{area}}} \tag{7}$$

The experimental data were fitted with a three-parameters power law by means of a least-square regression:

$$\Delta K = C_0 \cdot N^{C_1} + C_2 \tag{8}$$

Considering that the curve effectively represents the value of applied SIF range needed to observe the failure at a given fatigue life, Eq. (8) can be interpreted as a life-dependent threshold SIF range $\Delta K_{th}(N)$. Therefore, the authors suggested the formulation of an equivalent El-Haddad term which is a function of the considered fatigue life:

$$\sqrt{\text{area}}_0(N) = \frac{1}{\pi}\left[\frac{\Delta K_{th}(N)}{Y \cdot \Delta\sigma_0(N)}\right]^2 \tag{9}$$

in which $\Delta\sigma_0(N)$ is the fatigue strength of the defect-free material obtained from the Wöhler curve. As a result, the KT diagram is formulated as:

$$\Delta\sigma(N) = \Delta\sigma_0(N)\sqrt{\frac{\sqrt{\text{area}}_0(N)}{\sqrt{\text{area}}_0(N) + \sqrt{\text{area}}}} \tag{10}$$

The visualization of the three series of Ti-6Al-4V fatigue specimens in the ΔK-N plot is reported in Fig. 4. The regression line was determined by least-square fit of Eq. (8), with values $C_0 = 68696$ MPa $\sqrt{\text{mm}}$, $C_1 = -0.564$ and $C_2 = 114.39$ MPa $\sqrt{\text{mm}}$.

3.3. Fatigue strength model proposed by Shiozawa

With their fatigue strength model, Shiozawa and Lu [27,28] correlated the initial applied SIF range to the ratio between fatigue cycles and initial defect size $\sqrt{\text{area}}_i$ employing the two coefficients C and m of the Paris–Erdogan law:

$$\Delta K = \left[\frac{C(m-2)}{2}\right]^{-1/m} \cdot \left(\frac{N_f}{\sqrt{\text{area}}_i}\right)^{-1/m} = K'_f \cdot \left(\frac{N_f}{\sqrt{\text{area}}_i}\right)^{d'} \tag{11}$$

under the assumption that $\sqrt{\text{area}}_i \ll \sqrt{\text{area}}_f$. Tenkamp et al. [29] derived the two parameters of the equation by fitting the experimental results, hence neglecting the link with FCG coefficients.

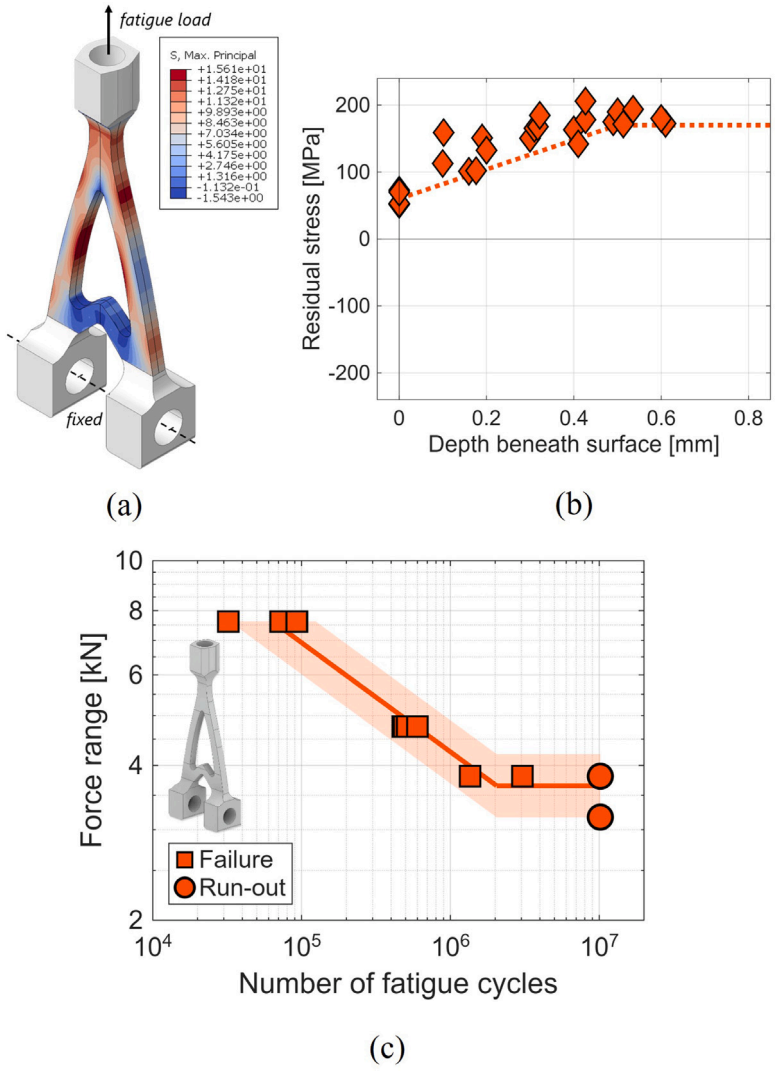

Fig. 2. Input data for the analyses of the first series of AlSi10Mg components, collected from [53]: (a) geometry of the component and stresses for a 1 kN tensile load from FE analysis; (b) residual stresses measured by X-ray diffraction beneath the surface; (c) results of the fatigue tests at load ratio $R = 0.1$.

With regards to Ti-6Al-4V specimens, all the series of fatigue samples were employed to derive the parameters of the Shiozawa curve. The experimental failures were fitted by the three-parameters maximum likelihood method to estimate the parameters of the log-normal function linking ΔK to the applied ${}^{N_f}/\sqrt{\text{area}}$ [57]. The resulting equation is:

$$\Delta K = 16496 \cdot \left(\frac{N_f}{\sqrt{\text{area}}} \right)^{-0.3085} \tag{12}$$

The use of the maximum likelihood method also permitted to derive the scatter of the fit, expressed in logarithmic terms as $\sigma_{\log(\Delta K)} = 0.5525$. The experimental points and the curve fit are shown in Fig. 5.

The formulation of the model does not include a threshold condition to describe the fatigue limit of the material [30]. Consequently, Fig. 5 shows that all run-out tests fall outside the 95% scatter band. This indicates the need of adding a fatigue limit to the original model.

3.4. Fatigue strength model by explicit FCG

The assessment of defects through FCG was achieved by the integration of the NASGRO equation for crack growth rate (13) coupled with the definition of SIF threshold (14):

$$\frac{da}{dN} = C\left[\left(\frac{1-f_N}{1-R}\right)\Delta K\right]^m \frac{\left(1-\frac{\Delta K_{\text{th}}}{\Delta K}\right)^p}{\left(1-\frac{K_{max}}{K_{Ic}}\right)^q} \tag{13}$$

$$\Delta K_{\text{th}} = \begin{cases} \Delta K_1 \sqrt{\frac{\sqrt{\text{area}}}{\sqrt{\text{area}}+\sqrt{\text{area}_0}}} \frac{\left(\frac{1-R}{1-f_N}\right)^{(1+R\cdot C_{\text{th}}^-)}}{(1-A_0)^{(C_{\text{th}}^+ - R\cdot C_{\text{th}}^-)}} & \text{if } R < 0 \\ \Delta K_1 \sqrt{\frac{\sqrt{\text{area}}}{\sqrt{\text{area}}+\sqrt{\text{area}_0}}} \frac{\left(\frac{1-R}{1-f_N}\right)^{(1+R\cdot C_{\text{th}}^+)}}{(1-A_0)^{(1-R)\cdot C_{\text{th}}^+}} & \text{if } R \geq 0 \end{cases} \tag{14}$$

The coefficients C, m, p, q, ΔK_1, C_{th}^+ and C_{th}^- were tuned from the experimental data, whereas the crack closure function f_N was computed with the equations proposed by Newman [58], therefore function of the constraint factor α, of the stress ratio R, and of the ratio between the maximum stress and the flow stress σ_{flow}, defined as the average between material yield strength and UTS. With reference to Ti-6Al-4V alloy, single edge-notch bend specimens were adopted to determine the FCG performance of the material [51]. Crack propagation tests with compression pre-cracking followed by the load reduction procedure aimed to determine the long crack SIF threshold ($\Delta K_{\text{th,LC}}$) at four

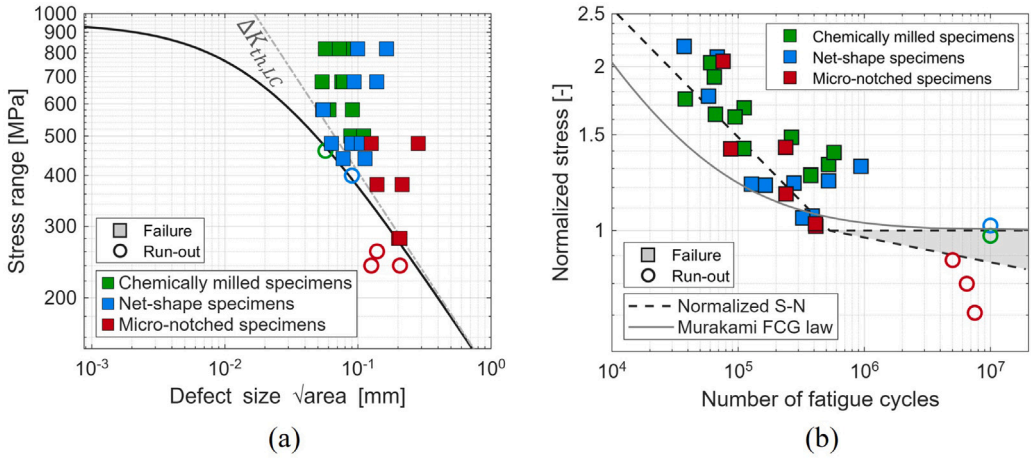

Fig. 3. Normalized S–N approach applied to the three series of Ti-6Al-4V fatigue tests: (a) KT diagram with the three sets of experimental points, the El-Haddad curve (black line) and the indication of $\Delta K_{th,LC}$ line; (b) normalized S–N curve and Murakami's FCG law, with the gray region indicating the use of a double-slope S–N curve to account for the very-high cycle fatigue behaviour of the material.

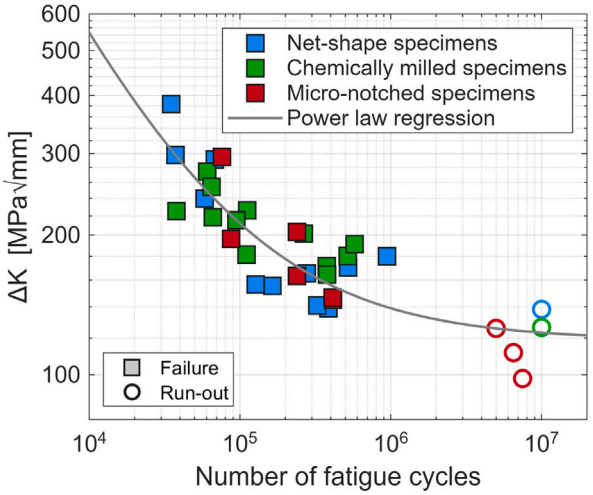

Fig. 4. K–N diagram of the three series of Ti-6Al-4V fatigue tests fitted with a power law.

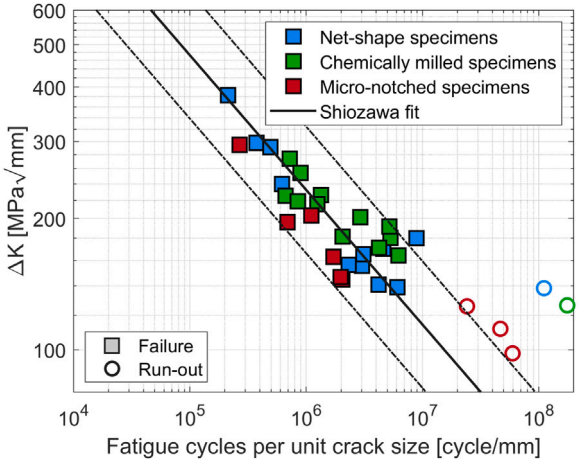

Fig. 5. Experimental results of the three series of Ti-6Al-4V fatigue tests displayed as proposed by the Shiozawa model, with indication of the fit and 95 % scatter band.

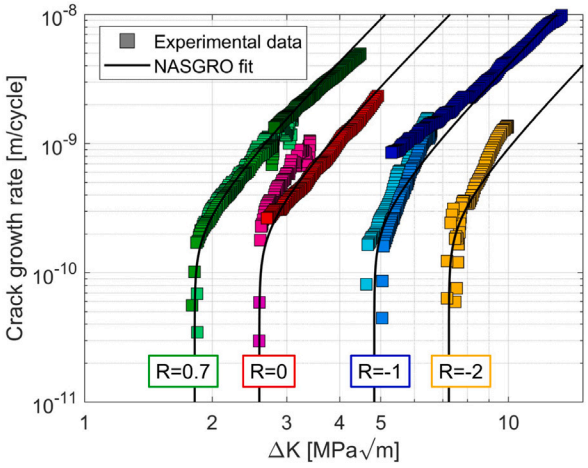

Fig. 6. FCG properties of Ti-6Al-4V adopted for this analysis, from [51].

stress ratios R (0.7, 0, −1 and −2). Additionally, compression pre-cracking constant amplitude tests were employed to characterize the Paris region. The results were fitted with the NASGRO model for crack propagation and are illustrated in Fig. 6.

The fatigue life was calculated by integrating Eq. (13) with NASGRO software [59] from a semi-elliptical surface anomaly with AR = 0.2 in a circular section with a diameter of 6 mm (using the crack case SC35 of NASGRO software).

3.5. Life predictions of Ti-6Al-4V fatigue specimens

The fatigue behaviours estimated with the discussed approaches are compared in the following with the experimental data from the three series of Ti-6Al-4V fatigue specimens. The average defect conditions, both in terms of $\sqrt{area}$ and AR, are considered in the prediction of the S–N curves. To improve the original Shiozawa model, a fatigue limit condition with the El-Haddad's threshold was added to the original model as suggested by Minerva et al. [57].

Fig. 7 shows the curves generated with the different models for each sample type. The S–N curves resulting from the various approaches show important differences.

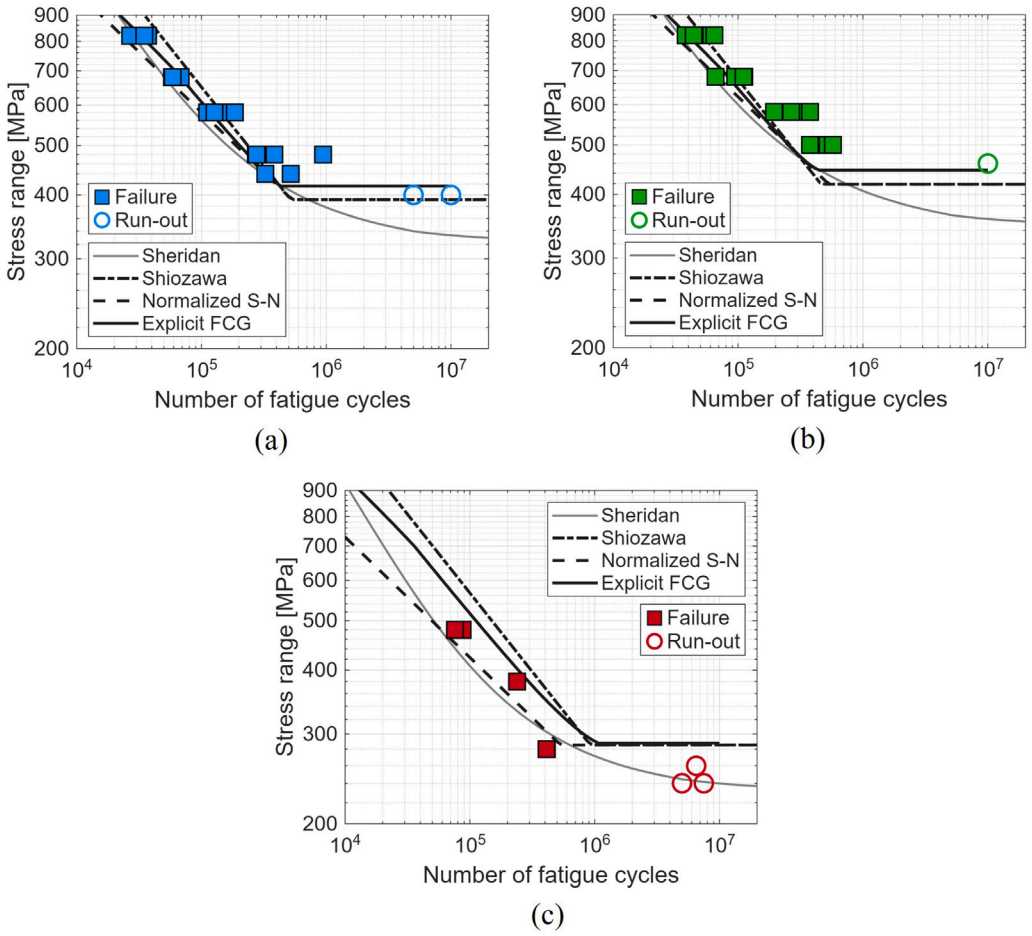

Fig. 7. Comparison among estimated S–N curves with different fatigue strength model and experimental data for Ti-6Al-4V specimens with: (a) net-shape surface; (b) chemically milled surface; (c) presence of micro-notch.

The Sheridan model deviates the most from the other cases because of the curved behaviour in the prediction, which lacks a proper knee point in the S–N diagram. Generally, all the implemented approaches provide a good description of the finite life region, albeit with small differences in slope. The Shiozawa model, for instance, produces a steeper representation of the linear S–N dependency, causing overestimation of the fatigue life at high stress levels.

Concerning the fatigue limit region, the predictions across the three series are mildly scattered:

- The explicit FCG method accurately estimates the fatigue limit for the net-shape and chemically milled specimens, whereas the prediction is overestimated with micro-notched samples;
- The normalized S–N and the Shiozawa methods share the same fatigue limit estimation from the El-Haddad model, which is slightly conservative for the net-shape and chemically milled series;
- The Sheridan method is strongly conservative for the net-shape and chemically milled series, while it accurately estimates the fatigue limit of the micro-notched samples.

The knee point of the S–N curves predicted by the analysed models shows some differences. The normalized S–N estimate, in fact, maintains a fixed N_k across the three series of specimens; on the contrary, both the Shiozawa and the explicit FCG approaches compute a value of N_k which is dependent on the average defect size of the considered series.

Fig. 8 adds a further comparison among the four models, showing the correlation between the experimental and predicted life of the Ti-6Al-4V specimens above the fatigue limit. Each graph shows the error of the prediction in terms of a diagram N_{exp}–N_{calc}, where the equity line represents the condition of a null error ($N_{calc} = N_{exp}$).

The data for the different assessment methods were analysed, similarly to the workflow in ASTM E3023 standard [60], through the calculation of the error as:

$$\begin{cases} \text{bias} = \sum_i \dfrac{\varepsilon_i}{N} \\ \sigma_\varepsilon = \sqrt{\dfrac{\sum_i (\varepsilon_i - \text{bias})^2}{N-2}} \end{cases} \tag{15}$$

where $\varepsilon = \log_{10}(N_{exp}) - \log_{10}(N_{calc})$ and σ_ε is the scatter of the predictions. The two quantities described in (15) are reported in Table 2.

The comparison between the experimental and estimated lives highlights the good accuracy of the Shiozawa and explicit FCG models, in which the dispersion of estimates is limited. The Shiozawa method develops a small bias, with the fit of the predictions following the equity case; on the other hand, for the explicit FCG method the conservatism is more pronounced. This difference could be ascribed to the crack nucleation, which is intrinsically included in the former model but is not present in the FCG analysis. Eventually, the Sheridan and normalized S–N models are affected by a larger conservatism of the prediction and a greater scatter σ_ε.

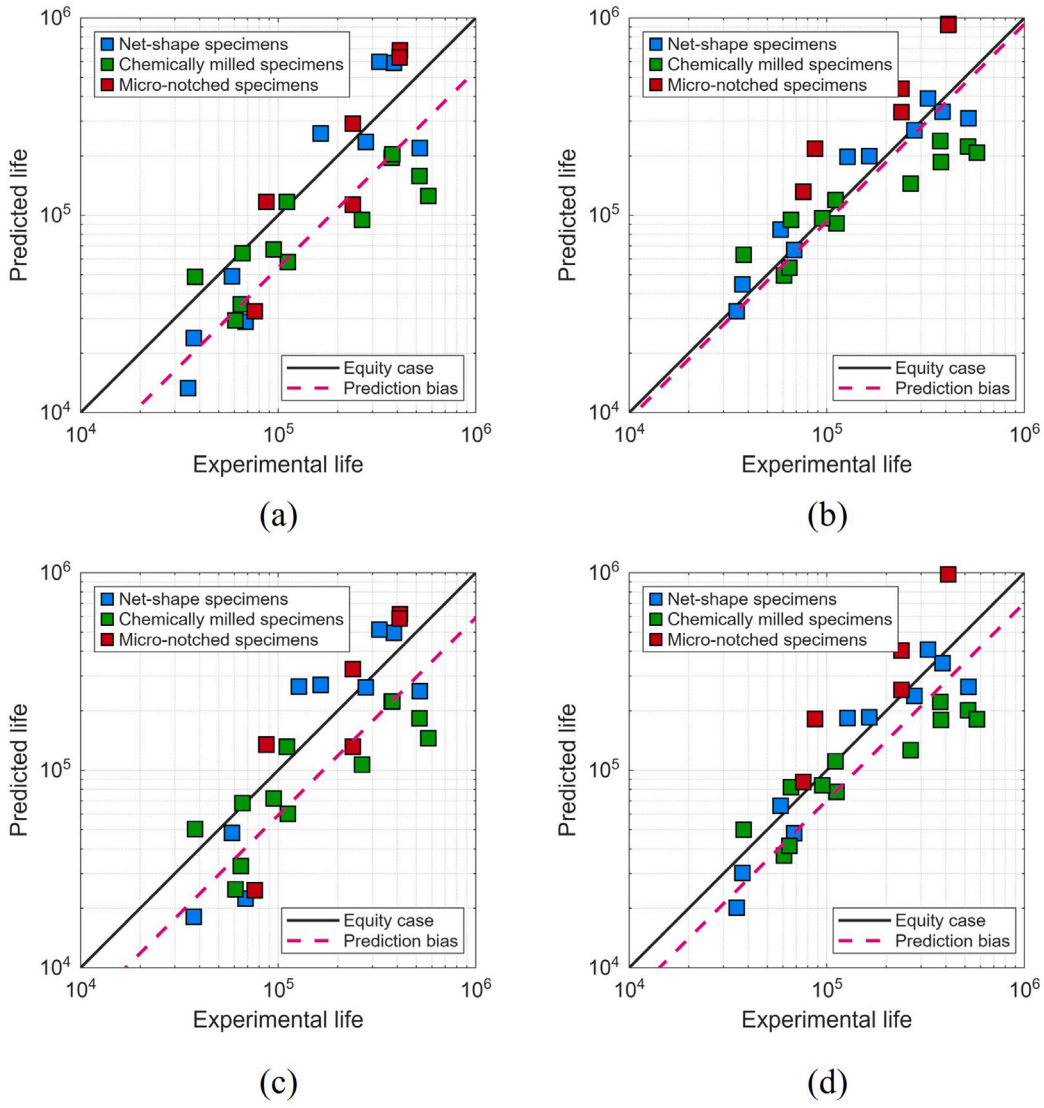

Fig. 8. Comparison between experimental and predicted life of Ti-6Al-4V fatigue specimens according to different strength models: (a) Sheridal model; (b) Shiozawa model; (c) normalized S–N model; (d) explicit FCG model.

Table 2
Bias and dispersion of the prediction models evaluated on Ti-6Al-4V fatigue specimens.

Fatigue strength model	bias	σ_ε	$CV_{\Delta\sigma_{w,0}}$
Sheridan	−45.8%	0.2149	0.107
Shiozawa	−6.9%	0.1611	0.080
Normalized S–N	−40.8%	0.2410	0.120
Explicit FCG	−29.7%	0.1689	0.084

4. Discussion

4.1. Critical defect maps

The visualization of fatigue strength models through prospective S–N curves permits the comparison with experimental data. However, the prime purpose of these approaches is the determination of critical flaw size curves for the assessment of AM components under fatigue loading. These curves represent, similarly to the KT diagram for the fatigue limit condition, the relationship between the applied stress range and the defect size for different prospective fatigue lives.

The maps, shown in Fig. 9, are referred to a semi-elliptical surface anomaly with AR = 0.2 in a Ti-6Al-4V specimen with dimensions 6 mm × 6 mm (SIF very close to the one of shallow crack in a circular section [61]), loaded at $R = -1$. To ease the visualization and comparison, the critical defect size curves are displayed for five different fatigue lives spanning from 5×10^4 to 1×10^6 cycles.

All the fatigue strength models employed in Fig. 9 express their distinct features in the critical defect maps: considering the graphs, it can be immediately seen that the Shiozawa model (as already shown in similar maps in [30]) does not show any flattening towards the high stress levels, while the other models tend towards fatigue life of defect-free material. The upper regions of the graphs for the Sheridan approach (Fig. 9a) and for explicit FCG algorithm (Fig. 9d) are very similar, especially for small number of fatigue cycles. On the other hand, the normalized S–N approach (Fig. 9c) tends to have a slightly wider vertical spacing among the different values of N_f.

The graphs in Fig. 9 also indicate the differences in the transition from the LEFM-driven failures, characterized by low stress levels and large anomaly sizes, to the failures led by microstructure, i.e. the upper region of the KT diagram:

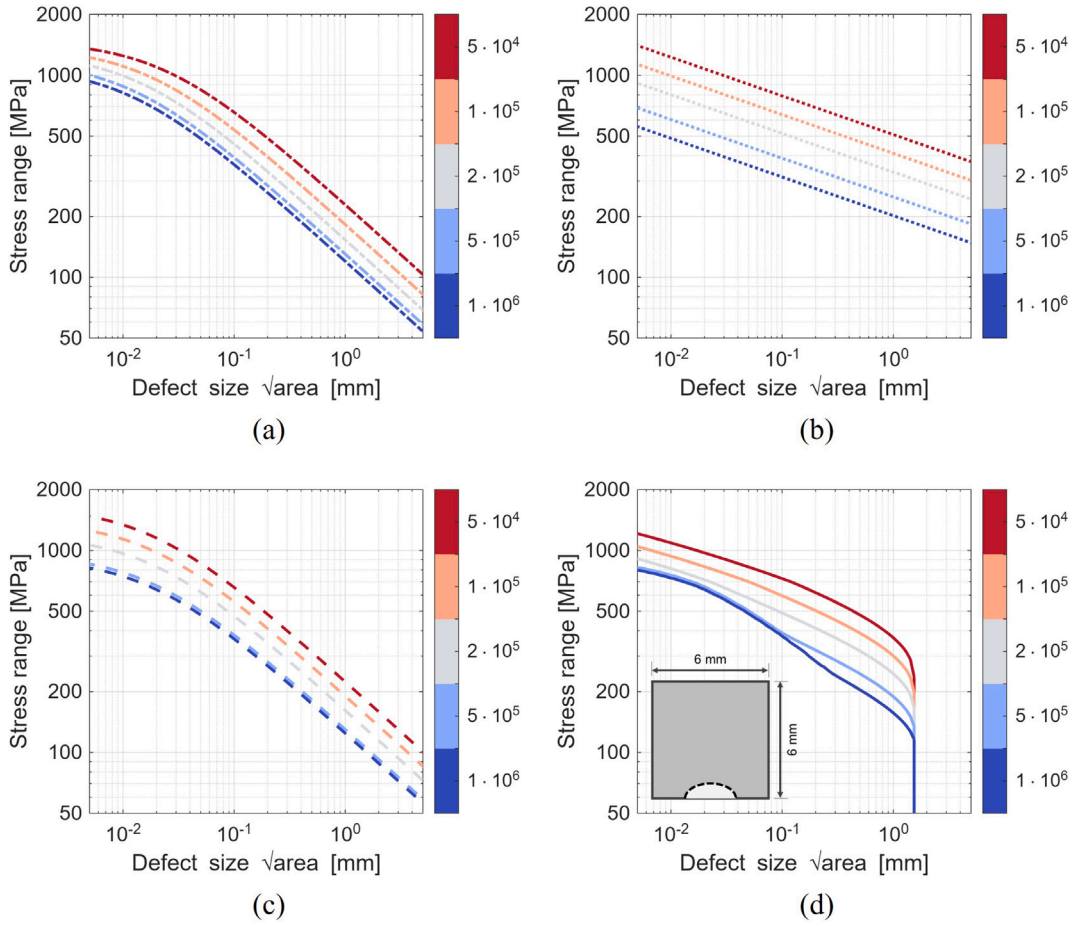

Fig. 9. Critical defect curves at different number of cycles to failure for the Ti-6Al-4V alloy: (a) Sheridan model; (b) Shiozawa model; (c) normalized S–N model; (d) explicit FCG model.

- The normalized S–N approach identifies a constant $\sqrt{\text{area}}_0$ for the transition (i.e., the curves are moving vertically);
- The Sheridan model has a life-dependent transition, as the term $\sqrt{\text{area}}_0$ is function of the target fatigue cycles (9);
- The approach based on explicit FCG does not have an analytical transition (except for fatigue limit where the threshold is described by the El-Haddad model), nevertheless the effect is visible on the critical defect curves at shorter fatigue lives.

However, the most relevant feature of the explicit FCG approach is that it considers an upper bound in the critical defect size, which corresponds to the geometrical constraint of the section in which the propagation occurs. As an example: at a $\Delta\sigma = 100\,\text{MPa}$ and for a target life of 1×10^5 cycles, the normalized S–N and Sheridan models would respectively predict a critical defect size $\sqrt{\text{area}} > 5\,\text{mm}$, while for direct FCG the maximum allowable defect cannot exceed 2 mm. This unique feature of direct FCG permits to determine a critical flaw size (or alternatively maximum allowable flaw size), which is bounded not to exceed a significant portion of the considered section.

4.2. Comparison among fatigue strength models

In light of the results from the life estimates and the generation of the critical defect curves, it is possible to observe the strengths and the critical points of the models.

Sheridan and Shiozawa models are entirely derived from the fit of the experimental points at a given stress ratio. This strongly limits the applicability of these approaches wherever the mean stress is not homogeneous, e.g. in presence of residual stress profiles. The normalized S–N model, instead, can be generalized to consider different stress ratios by introducing dependences of $\Delta\sigma_{w,0}$ and $\Delta K_{th,LC}$ on R: the former is determined by the Haigh diagram, the latter by Eq. (14). Therefore, the method can address the presence of residual stresses. In general, these three models benefit from their analytical relationships among stress–defect–life, which enable fast calculations of critical initial flaw sizes.

The explicit FCG model is well suited for variable stress ratios as it considers the effect of R in its constitutive equations; furthermore, residual stresses can be adequately considered using their profile beneath the surface in the propagation of cracks. Another strong benefit which is not shared with the other fatigue strength models is the possibility to adequately describe critical defects even in presence of finite geometries. On the other hand, though, the method requires a direct numerical integration of the non-linear crack propagation equation (13), which burdens the computational effort.

Table 3 summarizes the key advantages and critical points of each fatigue strength model, while also highlighting the requirements for the fit of parameters. Considering the accuracy of the life estimates of Ti-6Al-4V specimens, the critical defect size curves for the different approaches and balancing their key advantages and disadvantages, it is notable that the explicit FCG analysis offers the optimal result.

Table 3
Fatigue strength models compared by required input data, advantages and disadvantages.

Model	Parameters	Source	Main advantages	Main drawbacks
Normalized S–N	N_k, k_σ	Fatigue tests	Analytical formulation; critical defect curves linked to the El-Haddad parameter	S–N parameters fitted for a single R
	$\Delta\sigma_{w,0}$	Haigh diagram		
	$\Delta K_{th,LC}$	FCG tests for SIF threshold		
Sheridan	C_0, C_1, C_2	Fatigue tests and fractographies	Analytical formulation; critical defect curves linked to the El-Haddad parameter	K–N fit referred to observed defect sizes and not generalized for long cracks; conservative life estimates; parameters fitted for single R
	$\Delta\sigma_0$	S–N curve for defect-free material		
Shiozawa	K'_f, d'	Fatigue tests and fractographies	Analytical formulation; reduced scatter	Lack of a threshold condition; straight critical defect curves; parameters fitted for a single R
Explicit FCG	NASGRO parameters	FCG tests	Suitable for finite width geometry; applicable to different stress ratios	Computational effort; full characterization of FCG curves

5. Application to probabilistic analysis software

ProFACE software is a FE post-processing tool that performs probabilistic assessments of components containing material anomalies with fracture mechanics-based evaluations of the fatigue strength, employing a weakest-link model for the derivation of a global failure probability.

As a FE post-processor, ProFACE employs the applied stress tensor and the volume associated to each integration point of the model, with the scheme of the approach visualized in Fig. 10a. The calculation of the reliability $\mathcal{R}$ of each sub-volume V_i is calculated (see Fig. 10b) as:

$$\mathcal{R}_i = F_{max,V_i}(a_{crit,i}) \tag{16}$$

where $a_{crit,i}$ is calculated for the stress range ΔS_i at the sub-volume for a given target life and F_{max,V_i} has been estimated with the extreme value theory [62]. The software makes use of integration points as sub-volumes for volumetric defects and uses surface elements derived from element topology for surface features [50]. The analysis considers the scatter of the fatigue strength model $\Delta\sigma_w$, described through a log-normal distribution [49] with probability density function $f(\Delta\sigma_w)$. Eventually, the reliability can be calculated through a weakest-link as:

$$\mathcal{R} = \int \prod_i \mathcal{R}_i \cdot f(\Delta\sigma_w)\, \mathrm{d}\Delta\sigma_w \tag{17}$$

In the previous versions, ProFACE software used the normalized S-N diagram. In this study, the authors explore the use of the other presented fatigue strength models into the probabilistic analyses framework. In detail, the calculation of $a_{crit,i}$ in (16) was implemented with the same algorithms used for the critical defect maps.

5.1. Estimation of the scatter of the fatigue model

The probabilistic analysis via ProFACE software must capture all the sources of variability to establish accurate life estimates. The dispersion of the size of defects, included in ProFACE through the extreme value statistics, has to be combined with a dispersion $\sigma_{\log(\Delta\sigma_{w,0})}$ related to the fatigue strength model. This scatter indicates the inherent uncertainty of each model, which has no dependency on the size of anomalies.

The derivation of this inherent error for AlSi10Mg parts was discussed by Sausto et al. [50]; in their work, the scatter was simply taken as 0.03, a low value which corresponds the indications by ASTM E647 standard [63] for the variability of ΔK_{th}.

A precise evaluation of the uncertainty can be based on the comparison between predictions and experiments for fatigue specimens in which the defect size can be precisely measured (as shown in [23]). For the Ti-6Al-4V fatigue specimens, the authors employed σ_ε, determined within the N_{exp}–N_{calc} diagram and reported in Table 2. Since σ_ε is the uncertainty in terms of fatigue life, the values were divided by the slope k_σ of the S–N curve to obtain a variability of the fatigue strength $\sigma_{\log(\Delta\sigma_{w,0})}$ for the different models. This value was then transformed into a coefficient of variation $\mathrm{CV}_{\Delta\sigma_{w,0}}$ with:

$$\mathrm{CV}_{\Delta\sigma_{w,0}} = \sqrt{\exp\left(\sigma^2_{\log(\Delta\sigma_{w,0})}\right) - 1} \tag{18}$$

These values are reported in Table 2. This approach implies significant differences in scatter among the presented fatigue strength models, with the Shiozawa and explicit FCG methods maintaining a lower $\sigma_{\log(\Delta\sigma_{w,0})}$.

5.2. Implementation of explicit FCG life model to ProFACE software

As mentioned, the explicit FCG equations cannot be solved analytically due to the non-linearity of the problem, hence the necessity to build a material database to be looked up within the calculations. A material database is constructed by a set of S–N curves considering multiple initial crack sizes. The S–N curves are obtained with the integration, by forward Euler method, of the explicit FCG equation presented in Section 3.4.

The fatigue life is determined considering two types of defects, surface and embedded, located in sections with finite width (w) and thickness (t). The applied SIF is evaluated with the solutions by Newman and Raju [64] under a constant applied stress for the cases that do not present residual stresses. In presence of residual stresses acting on surface cracks, instead, the weight functions by Wang and Lambert [65,66] are adopted, as they allow the definition of the SIF from a non-uniform stress profile (19):

$$\begin{aligned} K_a(a,\sigma(x)) &= \int_0^a \frac{2}{\sqrt{2\pi(a-x)}}\left[1+\sum_{i=1}^{3} M_{i,A}\left(1-\frac{x}{a}\right)^{i/2}\right]\cdot\sigma(x)dx \\ K_c(a,\sigma(x)) &= \int_0^a \frac{2}{\sqrt{2\pi x}}\left[1+\sum_{i=1}^{3} M_{i,B}\left(\frac{x}{a}\right)^{i/2}\right]\cdot\sigma(x)dx \end{aligned} \tag{19}$$

where K_a and K_c are the SIF at the deepest point of the crack and at the surface points, while $M_{1,A}$, $M_{2,A}$, $M_{3,A}$, $M_{1,B}$, $M_{2,B}$ and $M_{3,B}$ are coefficients related to the AR of the crack and to a/t. At last, the term $\sigma(x)$ is the value of stress acting along the depth of the crack: by considering the cyclic stress S_{app} or the residual stress S_{RS}, it is possible to determine the applied SIF or the residual stress-induced SIF (K_{RS}). While the finite thickness is modelled in the coefficients of (19), the finite width was not expressed in the original formulation of the weight function. To overcome this effect, the authors applied a correction factor f_w to the SIF, expressed in (20), which was based on the proximity factor by Feddersen [67].

$$f_w = \frac{1}{\sqrt{1-\frac{2c}{w}}} \tag{20}$$

An important assumption concerns the location of the crack, as for both cases the initial crack is centred in the section (see Fig. 11). Conversely,

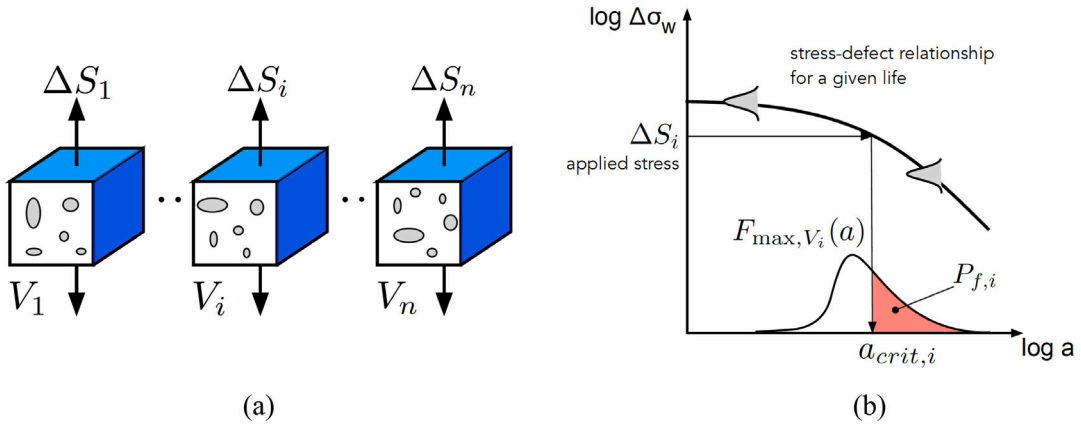

Fig. 10. Calculation of the probability of failure by ProFACE software: (a) scheme of the weakest-link model for the calculation of the reliability of each sub-volume; (b) failure probability associated to each sub-volume.

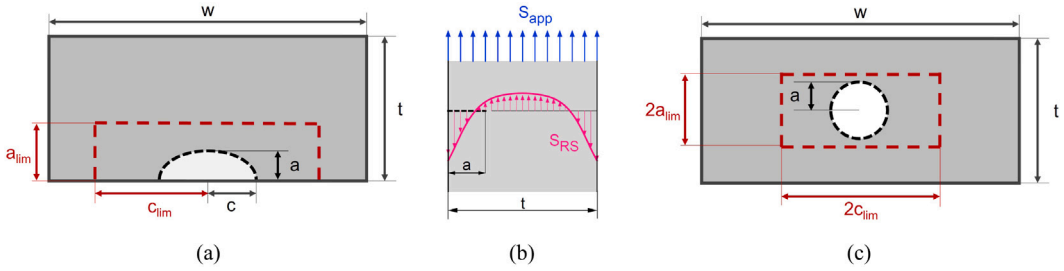

Fig. 11. Schematization of the geometry in the explicit FCG model for the different crack types: (a) surface cracks; (b) surface cracks in presence of residual stresses; (c) embedded cracks.

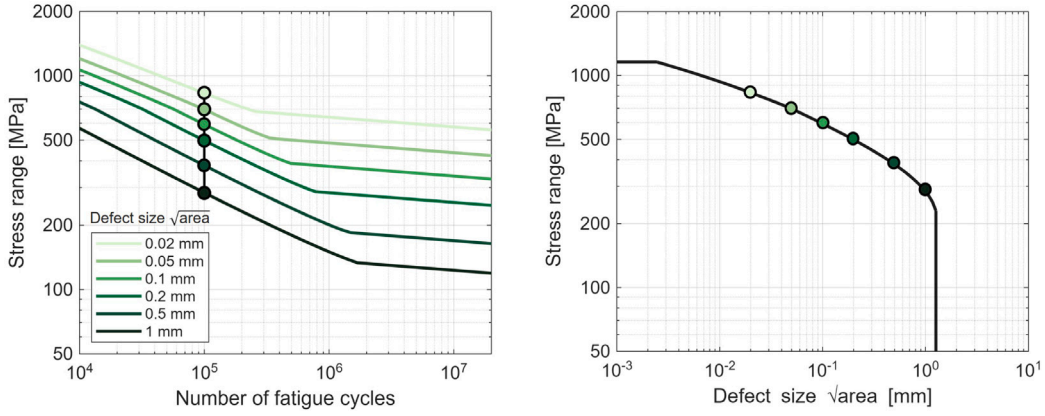

Fig. 12. Material database from the explicit FCG method: (a) generation of S–N curves for different initial flaw sizes and their interpolation at a target life; (b) creation of the critical defect map for the target life.

the two crack types differ from the initial AR, which is fixed to 1 for the embedded case while it is defined in the range 0.2 to 5 for the surface case.

The actual calculation of the fatigue cycles to failure is performed with a step-wise integration of Eq. (13), exploring a given range of initial crack sizes and adopting the local effective stress ratio R_{eff} computed as:

$$R_{\text{eff}} = \frac{K_{min} + K_{RS}}{K_{max} + K_{RS}} \tag{21}$$

The propagation is conducted along the two axes of the ellipse (embedded crack) or semi-ellipse (surface crack). It was chosen to maintain a fixed advancement step and to compute the number of

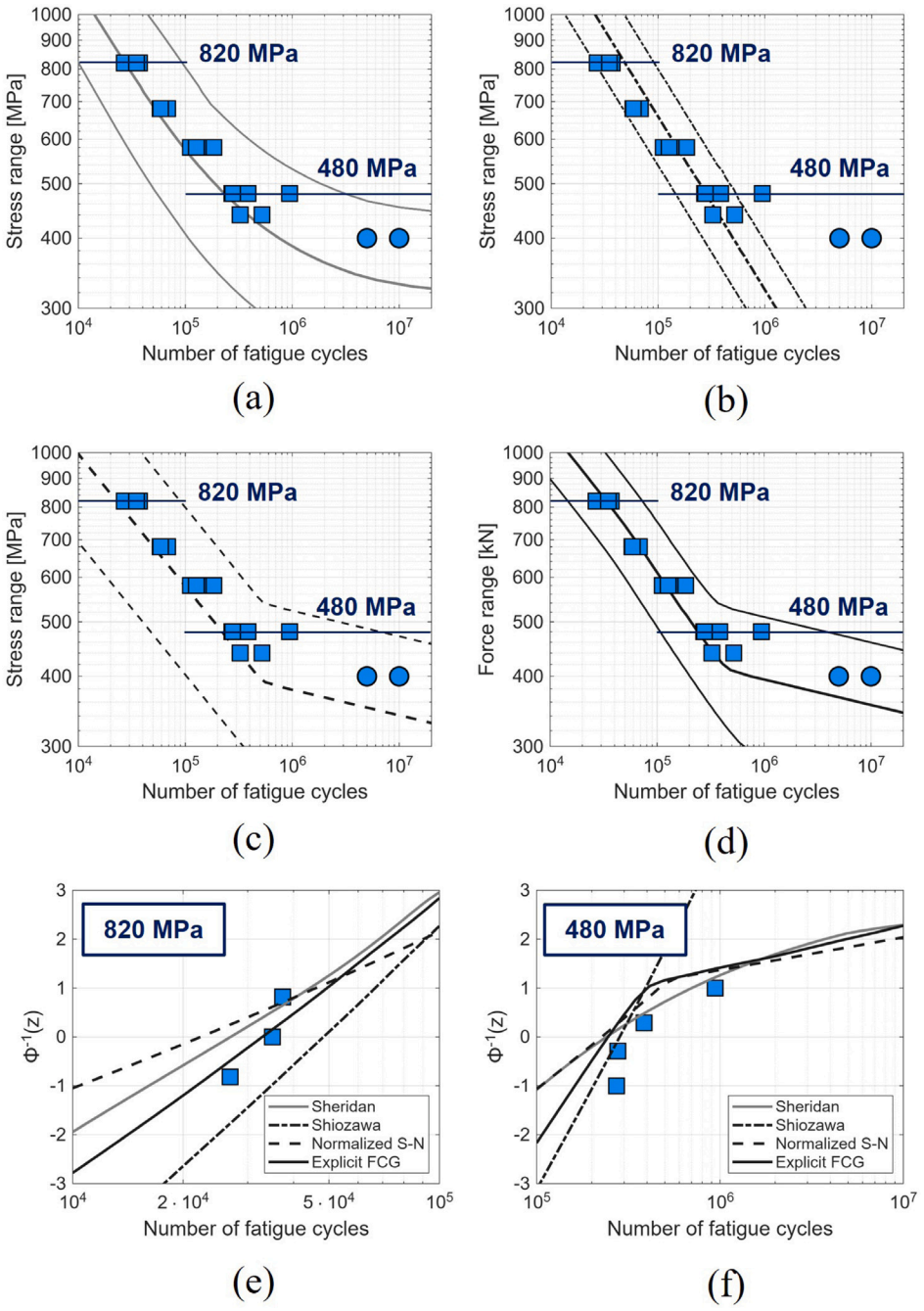

Fig. 13. Results of the probabilistic analyses of Ti-6Al-4V fatigue specimens with net-shape surface condition: (a) Sheridan model; (b) Shiozawa model; (c) normalized S–N model; (d) explicit FCG model. Log-normal probability charts of the failure probability reported: (e) at 820 MPa stress range; (f) at 480 MPa stress range.

cycles that leads to the set advancement; this propagation step was set to $10^{-3} \cdot t$.

Eventually, the arrest of the propagation is determined when one of the following conditions is met:

- $\frac{2c}{w} = 0.5$, being the limit condition of the weight function by Newman and Raju (Fig. 11);
- $\frac{a}{t} = 0.33$ for surface cracks, approximately corresponding to the limit condition on the width for an iso-K crack, and $\frac{a}{t} = 0.5$ for embedded cracks, being the limit condition of the weight function by Newman and Raju (Fig. 11);
- $\frac{K_{max}}{K_{Ic}} = 0.7$, indicating the imminent static failure from the fracture toughness of the material;
- $\frac{\sigma_{\text{net,max}}}{\sigma_{\text{flow}}} = 0.9$, to model the plastic collapse for the exceedance of the flow stress by the maximum stress on the net section containing the crack.

To ensure a sufficient accuracy without burdening the computational time, the authors chose to perform the calculations considering the following discretization steps:

- The values of initial crack sizes are 100 and range from a minimum size derived from Eq. (7) considering $\Delta K_{\text{th,LC}}|_{R=0.7}$ (i.e., the

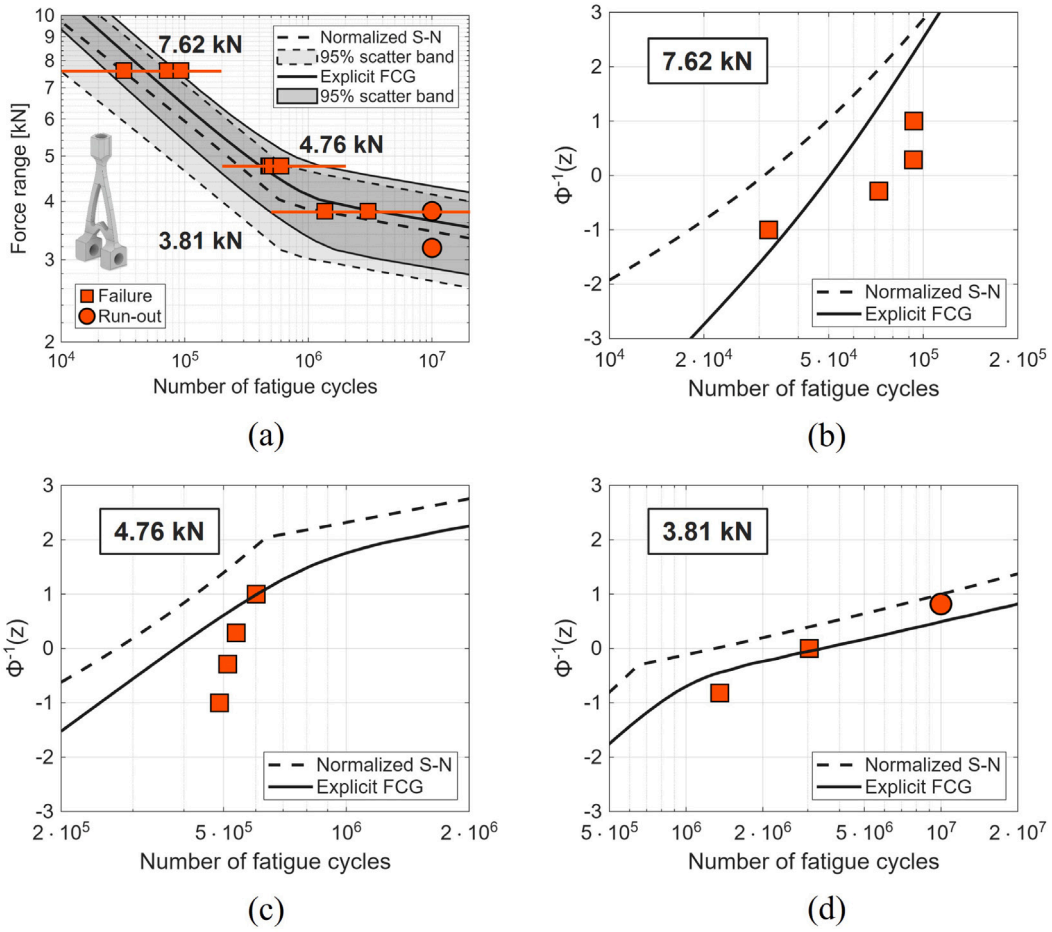

Fig. 14. Probabilistic analyses of the net-shape AlSi10Mg components with the normalized S–N and explicit FCG methods: (a) predicted fatigue life; (b) probability charts at 7.62 kN force range; (c) probability charts at 4.76 kN force range; (d) probability charts at 3.81 kN force range.

smallest threshold SIF range from an experimental campaign) to a maximum size that coincides with the geometrical constraints discussed in the crack arrest conditions.

- The values of $\Delta\sigma$ are 200 and their boundaries are selected in relation to the defect sizes to produce valid S–N points; the lowest stress range corresponds to the fatigue limit related to the largest defect and the highest stress range is $0.9{\cdot}\sigma_{flow}$.

After the derivation of the fatigue curves, the software interpolates the database for the prescribed service life. The resulting $\Delta\sigma$ - $\sqrt{area}$ values constitute the critical defect map adopted by the software to derive the critical initial flaw size. This process is illustrated in Fig. 12 for Ti-6Al-4V at $R = -1$ in absence of residual stresses, with relevant initial defect sizes and a target life of 1×10^5 cycles.

5.3. Probabilistic analyses of Ti-6Al-4V specimens

The Ti-6Al-4V fatigue specimens with net-shape and chemically milled surface conditions were analysed within a probabilistic assessment that considers the distribution of anomaly sizes and material properties presented in Section 2.1. The analyses excluded the micro-notched specimens because of the limited size of dataset and, as a consequence, the absence of a defect distribution.

Because of the lack of residual stresses altering the local stress ratio, all the presented fatigue strength models could be employed to characterize the fatigue resistance of the samples. In addition, the outcome of the probabilistic analyses was assessed by means of normal probability charts for $\log N$.

The outcome of the probabilistic analyses with the various methods is shown in Fig. 13. The prediction of fatigue cycles in the finite life region followed the same behaviour seen in the analyses with the average defect presented in Fig. 7: the 50% percentile of the Sheridan model in Fig. 13a slightly underestimates the fatigue life and the opposite trend is displayed by the Shiozawa model (Fig. 13b). The normalized S–N method in Fig. 13c and the explicit FCG method in Fig. 13d exhibit the most accurate representation of the 50% failure probability of both failed and run-out specimens. Similar conclusions could be drawn from the analyses of the chemically milled fatigue specimens.

The larger scatter σ_ϵ associated to the Sheridan and normalized S–N approaches, discussed in Section 3.5, is the main cause for the wider 95% scatter band observed in the probabilistic analysis; conversely, the Shiozawa and explicit FCG methods exhibit a narrower scatter.

The quality of the prediction with the explicit FCG method is also witnessed by the log-normal probability charts drawn for the stress range of 820 MPa (Fig. 13e) and for the stress range of 480 MPa (Fig. 13e). In both figures the experimental points are reported, and the predictions are scaled with the inverse of the log-normal cumulative distribution function evaluated at the resulting failure probability. The solid black line showing the outcome of the analysis with the explicit FCG model well captures the behaviour of the failures for the two stress levels considered.

5.4. Probabilistic analyses of the AlSi10Mg benchmark components

The analyses of AlSi10Mg components have substantial differences with respect to the Ti-6Al-4V specimens. The main contrast with the fatigue samples is the presence of a tensile residual stress state acting as a mean stress component superimposed to the fatigue cycles. Because of the local alteration of the stress ratio into R_{eff}, a probabilistic analysis with the use of the Sheridan or Shiozawa methods is impossible, given that the methods are tuned for a given stress ratio. Therefore, the authors present the assessment of these components on the ΔF–N diagram adopting the normalized S–N method and the explicit FCG method and imposing a value of $\mathrm{CV}_{\Delta\sigma_{\mathrm{w},0}}$ equal to 0.03 [50]. Again, the predictions of AlSi10Mg parts are assessed through probability charts for the log-cycles at all three load levels.

The behaviour of net-shape components is well described by the explicit FCG model, which accurately captures the fatigue life corresponding to the 50% failure probability at each tested stress level (Fig. 14a). The normalized S–N model, instead, predicts conservative fatigue cycles to failure in the finite life portion of the ΔF–N diagram. This result, which favours the explicit FCG analysis, is mainly ascribed to the possibility of handling the residual stress profile along the crack propagation, while only local residual stress value can be considered in the normalized S–N case. The probability charts in Fig. 14b-c-d confirm the good agreement of the explicit FCG model prediction.

6. Conclusions

In this work, the authors explored various fatigue strength model aiming to evaluate their performance in a defect tolerance assessment of AM parts. Four fracture mechanics-based fatigue strength models were compared in terms of predicted S–N curve from an average defect condition and in terms of critical flaw size curves. Their performance was evaluated in comparison with a large experimental database of Ti-6Al-4V fatigue specimens in two surface conditions and with the presence of micro-notches. Finally, the authors presented the new probabilistic fatigue assessment procedure based on the explicit FCG method for the generation of critical defect curves, which were adopted for the calculation of the reliability of parts through the weakest-link theory. The procedure was therefore validated through the analysis of Ti-6Al-4V specimens and AlSi10Mg benchmark components. The results of this paper can thus be summarized as follows:

1. The Sheridan model established a conservative prediction of the Ti-6Al-4V fatigue specimens with net-shape and chemically milled surfaces, while it accurately modelled the micro-notch case. On the contrary, the S–N curves obtained with the Shiozawa model well fitted the experimental data in all cases with the exception of micro-notch samples.
2. The predictions with the normalized S–N curve and the explicit FCG analysis were coherent with experimental data, both for the finite life region and at the fatigue limit.
3. Critical defect size curves showed the intrinsic features of each fatigue strength model. The presence of a geometrical limit to the critical defect size, coupled with the accuracy along the KT diagram, explained the advantages of the explicit FCG algorithm.
4. The model based on FCG analysis was implemented in ProFACE software to create a material database that was employed to determine critical initial flaw sizes within probabilistic analyses of components.
5. The model was successfully validated on a series of PBF-LB parts (both specimens and components) and on two materials. The prediction of the 50 % failure probability well represented the experimental points in each tested scenario.

CRediT authorship contribution statement

Lorenzo Rusnati: Writing – original draft, Investigation, Data curation. **Giuliano Minerva:** Writing – original draft, Software, Methodology, Data curation. **Luca Patriarca:** Writing – review & editing, Methodology, Investigation, Data curation. **Stefano Miccoli:** Software, Methodology, Data curation. **Stefano Beretta:** Writing – review & editing, Validation, Resources, Project administration, Funding acquisition, Conceptualization.

Declaration of competing interest

The authors declare the following financial interests/personal relationships which may be considered as potential competing interests: Stefano Beretta reports financial support was provided by European Space Agency. If there are other authors, they declare that they have no known competing financial interests or personal relationships that could have appeared to influence the work reported in this paper.

Acknowledgements

The authors acknowledge that the project was developed within the call-off order of the European Space Agency (ESA/ESTEC) “ESA Additive Manufacturing Benchmarking”, contract number 4000133245/20/NL/AR/idb. The project has involved ESA/ESTEC, The Manufacturing Technology Centre (MTC) and Politecnico di Milano (PoliMi). The authors also acknowledge Tatiana Risposi for her contribution to the algorithm for the creation of the Ti-6Al-4V database and the testing of Ti-6Al-4V specimens.

Appendix. Data from experimental database

The experimental data for Ti-6Al-4V and AlSi10Mg test articles employed in this work were collected from [50,51,53]. The database of fatigue and fatigue crack growth experiments is reported in the followings. For both alloys, the adopted specimens were identical and are shown in Fig. A.15 (see Tables A.4–A.6).

Table A.4
Tensile properties of the alloys [51,53].

Material	UTS [MPa]	Yield strength [MPa]	Elongation at fracture [%]
Ti-6Al-4V	1187	1146	12.0
AlSi10Mg	469	258	8.3

Table A.5
NASGRO coefficients for the fatigue crack growth properties of the alloys [51,53]. Data are reported in m/cycle and MPa$\sqrt{\mathrm{m}}$.

Material	ΔK_1	C_{th}^{+}	C_{th}^{-}	C	m	p
Ti-6Al-4V	1.70	−0.0058	−0.082	6.997×10^{-11}	3.2	0.3
AlSi10Mg	1.07	−0.5408	0.124	1.05×10^{-9}	3.51	0.66

Table A.6
Fatigue parameters of the alloys [51,53].

Material	Part	R	N_k	k_σ
Ti-6Al-4V	Net-shape specimens	−1	629265	−4.53
	Chemically milled specimens	−1	580369	−4.71
AlSi10Mg	Net-shape specimens	0.1	3669710	−4.09
	Net-shape components	0.1	2045380	−4.71

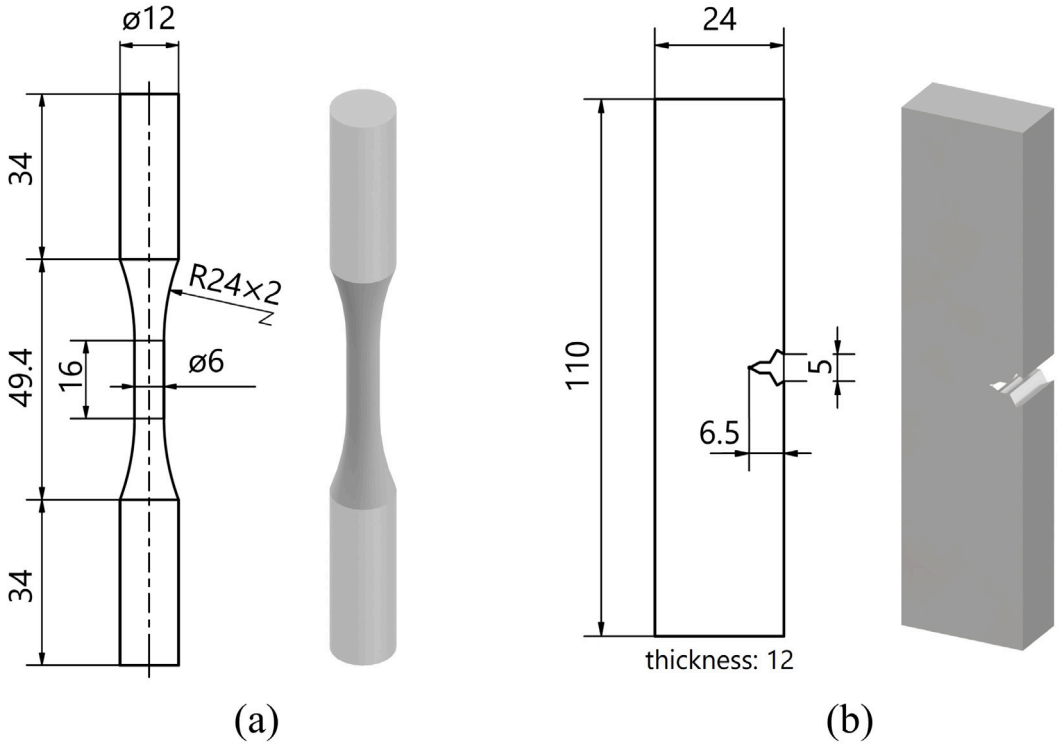

Fig. A.15. Technical drawings and 3D renderings of the Ti-6Al-4V specimens from [51,53]: (a) fatigue specimens; (b) crack propagation specimens.

Data availability

Data will be made available on request.

References

[1] Dutton B, Vesga W, Waller J, James S, Seifi M. Metal additive manufacturing defect formation and nondestructive evaluation detectability. ASTM Spec Tech Publ 2020;STP 1620:1–50. http://dx.doi.org/10.1520/STP162020180136.

[2] ASTM E3166-20e1. Standard guide for nondestructive examination of metal additively manufactured aerospace parts after build. 2020.

[3] ISO/ASTM TR 52905. Additive manufacturing of metals — Non-destructive testing and evaluation — Defect detection in parts. 2023.

[4] Mostafaei A, Zhao C, He Y, Ghiaasiaan SR, Shi B, Shao S, et al. Defects and anomalies in powder bed fusion metal additive manufacturing. Curr Opin Solid State Mater Sci 2022;26:100974. http://dx.doi.org/10.1016/J.COSSMS.2021.100974.

[5] Du C, Zhao Y, Jiang J, Wang Q, Wang H, Li N, et al. Pore defects in laser powder bed fusion: Formation mechanism, control method, and perspectives. J Alloys Compd 2023;944:169215. http://dx.doi.org/10.1016/J.JALLCOM.2023.169215.

[6] Sanaei N, Fatemi A. Analysis of the effect of surface roughness on fatigue performance of powder bed fusion additive manufactured metals. Theor Appl Fract Mech 2020;108:102638. http://dx.doi.org/10.1016/J.TAFMEC.2020.102638.

[7] Karakaş Ö, Kardeş FB, Foti P, Berto F. An overview of factors affecting high-cycle fatigue of additive manufacturing metals. Fatigue Fract Eng Mater Struct 2023;46:1649–68. http://dx.doi.org/10.1111/FFE.13967.

[8] Pegues J, Roach M, Williamson RS, Shamsaei N. Surface roughness effects on the fatigue strength of additively manufactured Ti-6Al-4V. Int J Fatigue 2018;116:543–52. http://dx.doi.org/10.1016/J.IJFATIGUE.2018.07.013.

[9] du Plessis A, Beretta S. Killer notches: The effect of as-built surface roughness on fatigue failure in AlSi10Mg produced by laser powder bed fusion. Addit Manuf 2020;35:101424. http://dx.doi.org/10.1016/J.ADDMA.2020.101424.

[10] Zerbst U, Bruno G, Buffière JY, Wegener T, Niendorf T, Wu T, et al. Damage tolerant design of additively manufactured metallic components subjected to cyclic loading: State of the art and challenges. Prog Mater Sci 2021;121:100786. http://dx.doi.org/10.1016/J.PMATSCI.2021.100786.

[11] Mukherjee T, DebRoy T. Mitigation of lack of fusion defects in powder bed fusion additive manufacturing. J Manuf Process 2018;36:442–9. http://dx.doi.org/10.1016/J.JMAPRO.2018.10.028.

[12] Zhang B, Meng WJ, Shao S, Phan N, Shamsaei N. Effect of heat treatments on pore morphology and microstructure of laser additive manufactured parts. Mater Des Process Commun 2019;1:e29. http://dx.doi.org/10.1002/MDP2.29.

[13] Gorelik M. Additive manufacturing in the context of structural integrity. Int J Fatigue 2017;94:168–77. http://dx.doi.org/10.1016/J.IJFATIGUE.2016.07.005.

[14] Wycisk E, Solbach A, Siddique S, Herzog D, Walther F, Emmelmann C. Effects of defects in laser additive manufactured Ti-6Al-4V on Fatigue Properties. Phys Procedia 2014;56:371–8. http://dx.doi.org/10.1016/J.PHPRO.2014.08.120.

[15] Beretta S, Romano S. A comparison of fatigue strength sensitivity to defects for materials manufactured by AM or traditional processes. Int J Fatigue 2017;94:178–91. http://dx.doi.org/10.1016/J.IJFATIGUE.2016.06.020.

[16] Kitagawa H, Takahashi S. Applicability of fracture mechanics to very small cracks or cracks in the early stage. Proceeding the Int Conf Mechanical Behav Mater 1976;627–31.

[17] Haddad MHE, Smith KN, Topper TH. Fatigue crack propagation of short cracks. J Eng Mater Technol 1979;101:42–6. http://dx.doi.org/10.1115/1.3443647.

[18] Murakami Y. Effects of small defects and nonmetallic inclusions on the fatigue strength of metals. JSME Int J Ser 1, Solid Mech Strength of Mater 1989;32(2):167–80. http://dx.doi.org/10.1299/jsmea1988.32.2_167.

[19] Merot P, Morel F, Pessard E, Mayorga LG, Buttin P, Baffie T. Fatigue strength and life assessment of L-PBF 316L stainless steel showing process and corrosion related defects. Eng Fract Mech 2022;276:108883. http://dx.doi.org/10.1016/J.ENGFRACMECH.2022.108883.

[20] Murakami Y. Metal fatigue: Effects of small defects and nonmetallic inclusions. Elsevier; 2002, p. 369.

[21] Murakami Y, Takagi T, Wada K, Matsunaga H. Essential structure of S-N curve: Prediction of fatigue life and fatigue limit of defective materials and nature of scatter. Int J Fatigue 2021;146:106138. http://dx.doi.org/10.1016/J.IJFATIGUE.2020.106138.

[22] Murakami Y, Endo M. Prediction model of S-N curve without fatigue test or with a minimum number of fatigue tests. Eng Fail Anal 2023;154:107647. http://dx.doi.org/10.1016/J.ENGFAILANAL.2023.107647.

[23] Romano S, Brückner-Foit A, Brandão A, Gumpinger J, Ghidini T, Beretta S. Fatigue properties of AlSi10Mg obtained by additive manufacturing: Defect-based modelling and prediction of fatigue strength. Eng Fract Mech 2018;187:165–89. http://dx.doi.org/10.1016/J.ENGFRACMECH.2017.11.002.

[24] Solberg K, Guan S, Razavi N, Welo T, Chan KC, Berto F. Fatigue of additively manufactured 316L stainless steel: The influence of porosity and surface roughness. Fatigue Fract Eng Mater Struct 2019;42:2043–52. http://dx.doi.org/10.1111/FFE.13077.

[25] Sheridan L, Gockel JE, Scott-Emuakpor OE. Stress-defect-life interactions of fatigued additively manufactured alloy 718. Int J Fatigue 2021;143:106033. http://dx.doi.org/10.1016/J.IJFATIGUE.2020.106033.

[26] Salvati E, Tognan A, Laurenti L, Pelegatti M, Bona FD. A defect-based physics-informed machine learning framework for fatigue finite life prediction in additive manufacturing. Mater Des 2022;222:111089. http://dx.doi.org/10.1016/J.MATDES.2022.111089.

[27] Shiozawa K, Lu L. Effect of non-metallic inclusion size and residual stresses on gigacycle fatigue properties in high strength steel. Adv Mater Res 2008;44–46:33–42. http://dx.doi.org/10.4028/WWW.SCIENTIFIC.NET/AMR.44-46.33.
[28] Shiozawa K, Lu L. Internal fatigue failure mechanism of high strength steels in gigacycle regime. Key Eng Mater 2008;378–379:65–80. http://dx.doi.org/10.4028/WWW.SCIENTIFIC.NET/KEM.378-379.65.
[29] Tenkamp J, Stern F, Walther F. Uniform fatigue damage tolerance assessment for additively manufactured and cast Al-Si alloys: An elastic-plastic fracture mechanical approach. Addit Manuf Lett 2022;3:100054. http://dx.doi.org/10.1016/J.ADDLET.2022.100054.
[30] Teschke M, Moritz J, Tenkamp J, Marquardt A, Leyens C, Walther F. Defect-based characterization of the fatigue behavior of additively manufactured titanium aluminides. Int J Fatigue 2022;163:107047. http://dx.doi.org/10.1016/J.IJFATIGUE.2022.107047.
[31] Stammkötter S, Tenkamp J, Teschke M, Donnerbauer K, Koch A, Platt T, et al. Fatigue and short crack assessment of powder bed fusion laser-based fabricated AlSi10Mg miniature specimens under alternating bending load. Mater Des 2024;247:113412. http://dx.doi.org/10.1016/J.MATDES.2024.113412.
[32] ECSS-E-ST-32-01C Rev1. Space engineering - fracture control. (6 March):2009, p. 1–84.
[33] NASA-STD-5019. Fracture control requirements for spaceflight hardware. 2020, National Aeronautics and Space Administration.
[34] Yadollahi A, Mahtabi MJ, Khalili A, Doude HR, Newman JC. Fatigue life prediction of additively manufactured material: Effects of surface roughness, defect size, and shape. Fatigue Fract Eng Mater Struct 2018;41:1602–14. http://dx.doi.org/10.1111/FFE.12799.
[35] Sanaei N, Fatemi A. Defect-based fatigue life prediction of L-PBF additive manufactured metals. Eng Fract Mech 2021;244:107541. http://dx.doi.org/10.1016/J.ENGFRACMECH.2021.107541.
[36] Kishore P, Singh T, Aher R, Alankar A. Workflow for fatigue life prediction of additive manufactured complex designs from powder bed fusion of Ti–6Al–4V. Int J Fatigue 2023;177:107941. http://dx.doi.org/10.1016/J.IJFATIGUE.2023.107941.
[37] Wang H, Gao SL, Wang BT, Ma YT, Guo ZJ, Zhang K, et al. Recent advances in machine learning-assisted fatigue life prediction of additive manufactured metallic materials: A review. J Mater Sci Technol 2024;198:111–36. http://dx.doi.org/10.1016/J.JMST.2024.01.086.
[38] Dong Y, Yang X, Chang D, Li Q. Predicting fatigue life of multi-defect materials using the fracture mechanics-based physics-informed neural network framework. Int J Fatigue 2025;190:108626. http://dx.doi.org/10.1016/J.IJFATIGUE.2024.108626.
[39] Balamurugan R, Chen J, Meng C, Liu Y. Probabilistic fatigue life prediction of AM-built alloy using physics-guided neural network. In: AIAA science and technology forum and exposition, AIAA scitech forum 2025. American Institute of Aeronautics and Astronautics Inc, AIAA; 2025, http://dx.doi.org/10.2514/6.2025-0822.
[40] Hu Y, She Y, Wu S, Kan Q, Yu H, Kang G. Critical physics-informed fatigue life prediction of laser 3D printed AlSi10Mg alloys with mass internal defects. Int J Mech Sci 2024;284:109730. http://dx.doi.org/10.1016/J.IJMECSCI.2024.109730.
[41] Wormsen A, Sjödin B, Härkegård G, Fjeldstad A. Non-local stress approach for fatigue assessment based on weakest-link theory and statistics of extremes. Fatigue Fract Eng Mater Struct 2007;30:1214–27. http://dx.doi.org/10.1111/J.1460-2695.2007.01190.X.
[42] Blacha L, Karolczuk A, Bański R, Stasiuk P. Application of the weakest link analysis to the area of fatigue design of steel welded joints. Eng Fail Anal 2013;35:665–77. http://dx.doi.org/10.1016/J.ENGFAILANAL.2013.06.012.
[43] Li P, Warner DH, Phan N. Predicting the fatigue performance of an additively manufactured Ti-6Al-4V component from witness coupon behavior. Addit Manuf 2020;35:101230. http://dx.doi.org/10.1016/J.ADDMA.2020.101230.
[44] Fjeldstad A, Wormsen A, Härkegård G. Simulation of fatigue crack growth in components with random defects. Eng Fract Mech 2008;75:1184–203. http://dx.doi.org/10.1016/J.ENGFRACMECH.2007.04.006.
[45] Wormsen A, Fjeldstad A, Härkegård G. A post-processor for fatigue crack growth analysis based on a finite element stress field. Comput Methods Appl Mech Engrg 2008;197:834–45. http://dx.doi.org/10.1016/J.CMA.2007.09.012.
[46] McClung RC, Enright MP, Millwater HR, Leveront G, Hudak S. A software framework for probabilistic fatigue life assessment of gas turbine engine rotors. In: Probabilistic aspects of life prediction. ASTM International; 2004.
[47] Millwater HR, Mcclung RC, Enright MP. A new tool for design and certification of aircraft turbine rotors. 2004, http://dx.doi.org/10.1115/1.1622409.
[48] Enright MP, McClung RC, Sobotka JC, Moody JP, McFarland J, Lee Y-D, et al. Influences of non-destructive inspection simulation on fracture risk assessment of additively manufactured turbine engine components. American Society of Mechanical Engineers Digital Collection; 2018, http://dx.doi.org/10.1115/GT2018-77058.
[49] Romano S, Miccoli S, Beretta S. A new FE post-processor for probabilistic fatigue assessment in the presence of defects and its application to AM parts. Int J Fatigue 2019;125:324–41. http://dx.doi.org/10.1016/J.IJFATIGUE.2019.04.008.
[50] Sausto F, Romano S, Patriarca L, Miccoli S, Beretta S. Benchmark of a probabilistic fatigue software based on machined and as-built components manufactured in AlSi10Mg by L-PBF. Int J Fatigue 2022;165:107171. http://dx.doi.org/10.1016/J.IJFATIGUE.2022.107171.
[51] Risposi T, Rusnati L, Patriarca L, Hardaker A, Luczyniec D, Beretta S. Fatigue of Ti6Al4V manufactured by PBF-LB: A comparison of failure mechanisms between net-shape and electro-chemically milled surface conditions. Eng Fail Anal 2025;172:109403. http://dx.doi.org/10.1016/J.ENGFAILANAL.2025.109403.
[52] Beretta S. Affidabilità delle costruzioni meccaniche. Springer; 2009.
[53] Beretta S, Patriarca L, Gargourimotlagh M, Hardaker A, Brackett D, Salimian M, et al. A benchmark activity on the fatigue life assessment of AlSi10Mg components manufactured by L-PBF. Mater Des 2022;218:110713. http://dx.doi.org/10.1016/J.MATDES.2022.110713.
[54] Dowling NE. Mechanical behavior of materials: Engineering methods for deformation, fracture, and fatigue. 4th ed.. Harlow: Pearson; 2013, p. 954.
[55] Sonsino CM. Course of SN-curves especially in the high-cycle fatigue regime with regard to component design and safety. Int J Fatigue 2007;29:2246–58. http://dx.doi.org/10.1016/J.IJFATIGUE.2006.11.015.
[56] Yamashita Y, Murakami Y. Small crack growth model from low to very high cycle fatigue regime for internal fatigue failure of high strength steel. Int J Fatigue 2016;93:406–14. http://dx.doi.org/10.1016/J.IJFATIGUE.2016.04.016.
[57] Minerva G, Awd M, Koch A, Walther F, Beretta S. Transferability of anomaly data to fatigue properties of PBF-LB AlSi10Mg parts with different volumes. Int J Fatigue 2025;195:108852. http://dx.doi.org/10.1016/J.IJFATIGUE.2025.108852.
[58] Newman JC. A crack opening stress equation for fatigue crack growth. Int J Fract 1984;24. URL https://ntrs.nasa.gov/citations/19840050000.
[59] South West Research Institute. NASGRO reference manual version 10.0. 2023.
[60] ASTM E3023-21. Standard practice for probability of detection analysis for â versus a data. 2021.
[61] Tatiana Risposi. Fatigue life assessment of AM components manufactured by L-PBF in Ti6Al4V. Politecnico di Milano; 2023.
[62] Beretta S. More than 25 years of extreme value statistics for defects: Fundamentals, historical developments, recent applications. Int J Fatigue 2021;151:106407. http://dx.doi.org/10.1016/j.ijfatigue.2021.106407.
[63] ASTM E647-24. Standard test method for measurement of fatigue crack growth rates. 2024.
[64] Newman JC, Raju IS. Stress-intensity factor equations for cracks in three-dimensional finite bodies subjected to tension and bending loads. 1984, URL https://ntrs.nasa.gov/citations/19840015857.
[65] Wang X, Lambert SB. Stress intensity factors for low aspect ratio semi-elliptical surface cracks in finite-thickness plates subjected to nonuniform stresses. Eng Fract Mech 1995;51:517–32. http://dx.doi.org/10.1016/0013-7944(94)00311-5.
[66] Wang X, Lambert SB. Stress intensity factors and weight functions for high aspect ratio semi-elliptical surface cracks in finite-thickness plates. Eng Fract Mech 1997;57:13–24. http://dx.doi.org/10.1016/S0013-7944(97)00018-0.
[67] Feddersen CE. Evaluation and prediction of the residual strength of center cracked tension panels. Damage Toler Aircr Struct 1971.